Applied Catalysis B: Environmental 340 (2024) 123278

Contents lists available at ScienceDirect

Applied Catalysis B: Environmental

journal homepage: www.elsevier.com/locate/apcatb

Dynamical transfer behavior and *in situ* interaction with H2O molecules of charge carriers over heterojunction in non-adiabatic systems

Menghan Gan [a], Shanshan Lai [a], Shujuan Jiang [a,*], Chuanzhi Sun [c,*], Shaoqing Song [b,*]

[a] School of Materials Science & Chemical Engineering, Ningbo University, Ningbo 330013, China
[b] School of New Energy, Ningbo University of Technology, Ningbo 315336, China
[c] College of Chemistry', Chemical Engineering and Materials Science, Shandong Normal University, Jinan 250014, China

ARTICLE INFO

Keywords:
Heterojunction
Localized field
Charge transfer behavior
In situ DRIFTS
Dynamic process

ABSTRACT

In adiabatic systems, both photocatalytic Z-scheme and S-scheme mechanisms are feasible. However, almost all photocatalysis are non-adiabatic, and the mechanisms need to be rationalized. Herein, CuS was *in-situ* grown at S locus of MoS_2, thus increasing their wave function overlapping to decrease the interface barrier. *In situ* DRIFTS and XPS, and Hall effect studies have found that Fermi levels are not equal at interfaces in non-adiabatic system, and consequently the internal electric fields are formed at interfaces and localized electric fields in bulk and on surface, which boost e^- and h^+ to transfer directionally to MoS_2 as reductive sites and CuS as oxidative sites for dehydrogenating * -OH and coupling * -O and releasing H_2 and O_2 with STH efficiency of 1.70%. In-depth insight into charge transfer behavior and dynamical reaction process over heterojunctions in non-adiabatic systems indicates the general validity of photocatalytic models and facilitates rational designs and photocatalysis principle understanding.

1. Introduction

Photocatalytic H_2O overall splitting into H_2 is considered one of the most promising applications for converting solar energy into green energy, since this energy conversion process does not require any strong acid/alkali electrolytes or external auxiliary biases [1–4]. Once the limitation of solar-to-H_2 conversion efficiency (STH) is overshot, it will inevitably affect the production mode of H_2 energy and even optimize the global energy pattern. Nowadays, many semiconductor photocatalysts, *e.g.*, TiO_2, CdS, MoS_2, CeO_2, g-C_3N_4, *etc*, have suitable band gaps with advantageous valence band and conduction band potentials for H_2O splitting, but demonstrate low STH efficiency. Studies have revealed that, H_2O splitting reaction is subject to two key dynamic processes: One is poor capabilities of charge spatial separation and directional transfer, and the other is high redox overpotentials for generating H_2 and O_2 [5–8]. Since Z- and S-scheme heterojunction photocatalytic principles for charge transfer behaviors and their reactions have been proposed to solve the above photocatalytic dilemmas, the two heterojunction principles have received widespread and strong attentions [9,10]. Z-, and S-scheme heterojunction photocatalysts are comprised of an oxidative-type semiconductor (OS) and a reductive-type semiconductor (RS) with sustainable internal electric field (IEF) generated by their Fermi level difference, and photon-irradiated electrons (e^-) from conduction band (CB) of OS recombine with holes (h^+) from valence band (VB) of RS across the interface under the IEF action [11,12]. As a result, e^- from RS and h^+ from OS with strong redox abilities will be well preserved, thus transferring to opposite directions with a long distance. Accordingly, these preserved energetic e^- and h^+ have great capabilities to overcome the high overpotentials for H_2O splitting reaction, and thus provide a powerful guarantee to satisfy the dynamics requirements by achieving two birds with one stone [13], which thus presents a great potential to enhance STH efficiency for photocatalytic H_2O overall splitting.

Nevertheless, the photocatalytic reaction mechanisms of Z- and S-scheme are feasible in adiabatic systems. In semiconductor physics, the Fermi level change, band bending and Fermi level flush of the RS and OS heterostructures at the interface are considered under adiabatic conditions [14,15]. However, almost all photocatalytic systems are non-adiabatic, and it is obvious that both of the two mechanisms need to be further rationalized. Most researchers consider that, Fermi energy levels are flush at the interface after RS and OS contact, which however needs to be argued in non-adiabatic system [16,17]; Besides, IEF formation at the interfaces of RS and OS is based on their Fermi level differences, which is a game process [18,19]. In addition, researchers

* Corresponding authors.
E-mail addresses: jiangshujuan@nbu.edu.cn (S. Jiang), suncz@sdnu.edu.cn (C. Sun), songshaoqing@nbut.edu.cn (S. Song).

https://doi.org/10.1016/j.apcatb.2023.123278
Received 17 June 2023; Received in revised form 6 August 2023; Accepted 7 September 2023
Available online 9 September 2023
0926-3373/© 2023 Elsevier B.V. All rights reserved.

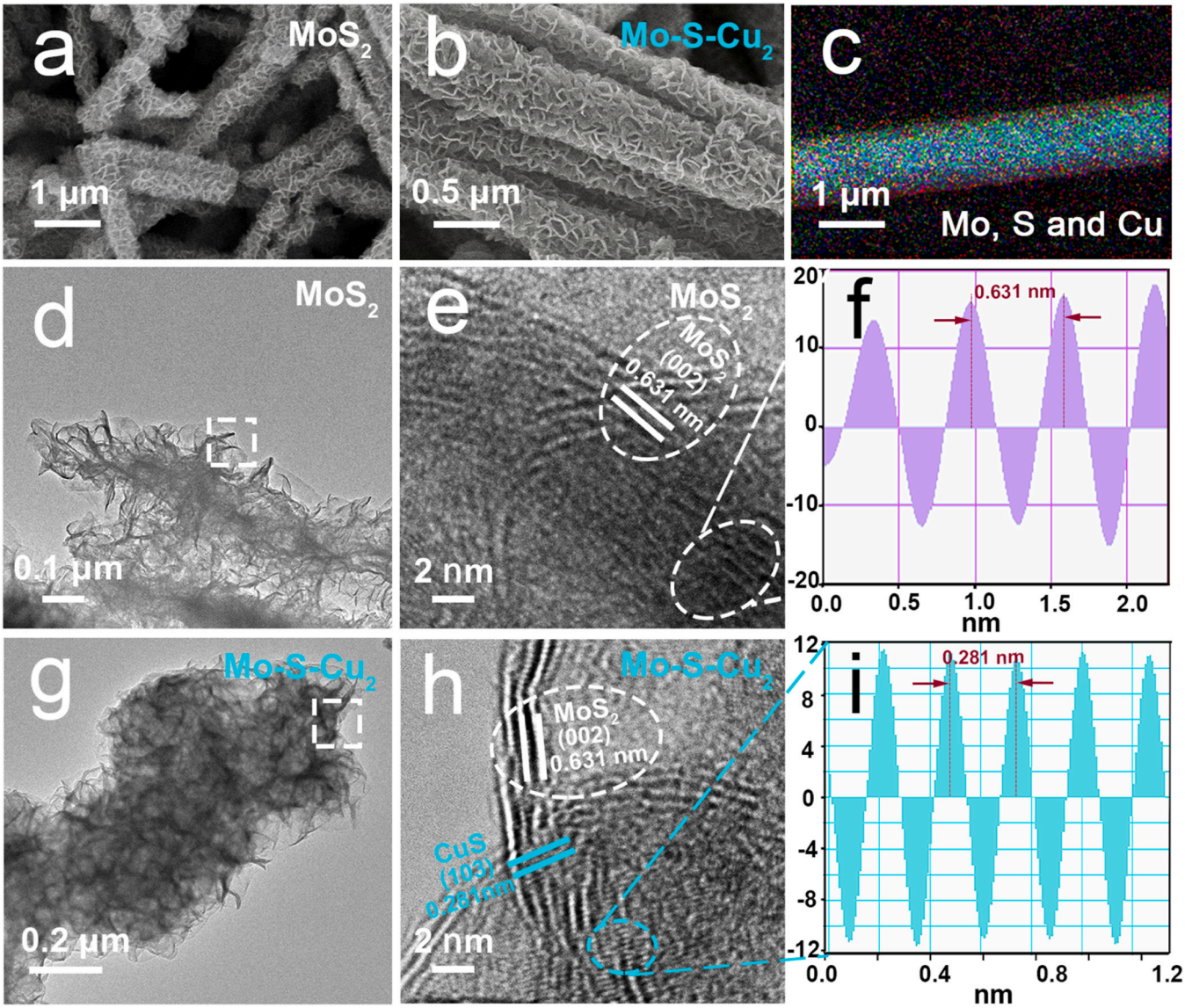

Fig. 1. (a&b) FESEM images for (a) MoS_2 and (b) Mo-S-Cu_2. (c) Element mapping for Mo-S-Cu_2 sample. (d-f) TEM (d,g) and HRTEM (e,h), and lattice fringes derived from HRTEM for MoS_2 and Mo-S-Cu_2 (f,i).

intuitively believe that electrons migrate directly from CB of the OS to VB of the RS and recombine holes through a Z-shaped path. However, electrons from OS first pass through the interfaces to RS under IEF action; based on the photomultiplier effect, electrons will be partially excited to the CB of RS and further used for photocatalytic reduction [20,21], rather than completely recombine with h^+. For almost all reported heterojunction photocatalysts, the fundamental challenge of high interface potential barriers hindering charge transfer through the interface has not yet been resolved. Since the spin directions of atoms from multi-component are the same in essence, the Pauli repulsion between electrons inhibits the overlap of wave function, which thus creates a large potential barrier for charge transfer at the phase interface [22,23].

Herein, CuS as OS was *in-situ* grown at S as charge transfer bridging from MoS_2 as RS for enhancing the overlap of wave functions and electron cloud density. *In-situ* X-ray photoelectron spectroscopy (XPS), Kelvin probe force microscopy (KPFM), Hall effect, *in-situ* diffuse reflectance infrared Fourier transform spectroscopy (*in-situ* DRIFTS), and photoelectric tests have confirmed that, Fermi level difference as cornerstone results in the formation of IEF at interfaces and localized electric field (LEF) on surface to promote the directional transfer of e^- and h^+ to MoS_2 as reductive site and CuS as oxidative site for H_2 and O_2 generation through * -OH dehydrogenation and subsequent * -O coupling. Photo-generated e^- from CuS are transported to reductive sites of MoS_2 where they are not completely recombined with h^+, but further utilized for photocatalytic H_2O reduction within the synergistic effect of IEF and LEF. Therefore, STH of 1.70% is achieved under AM 1.5 G irradiation.

2. Experimental sections

2.1. In situ construction of heterojunctions

1.78 mL of $C_2H_4(NH_2)_2$ was added into 30 mL of $(NH_4)_6Mo_7O_{24}\cdot 4H_2O$ solution (0.068 mol/L), and HCl (35 mL, 1 mol/L) was slowly dropped into the mixture solution, resulting in the generation of a white precipitate. After vacuum filtration and subsequent dehydration at 60 °C for 12 h, 0.2 g of sample was dispersed into sulfur source of L-cysteine solution (30 mL, 0.156 mol/L) with the aid of ultrasonication, and the mixed solution was then transferred into a Teflon-lined autoclave and kept at 200 °C for 14 h, and spontaneously cooled to room temperature. By cleaning and drying treatment, the obtained pristine MoS_2 (3 mg)

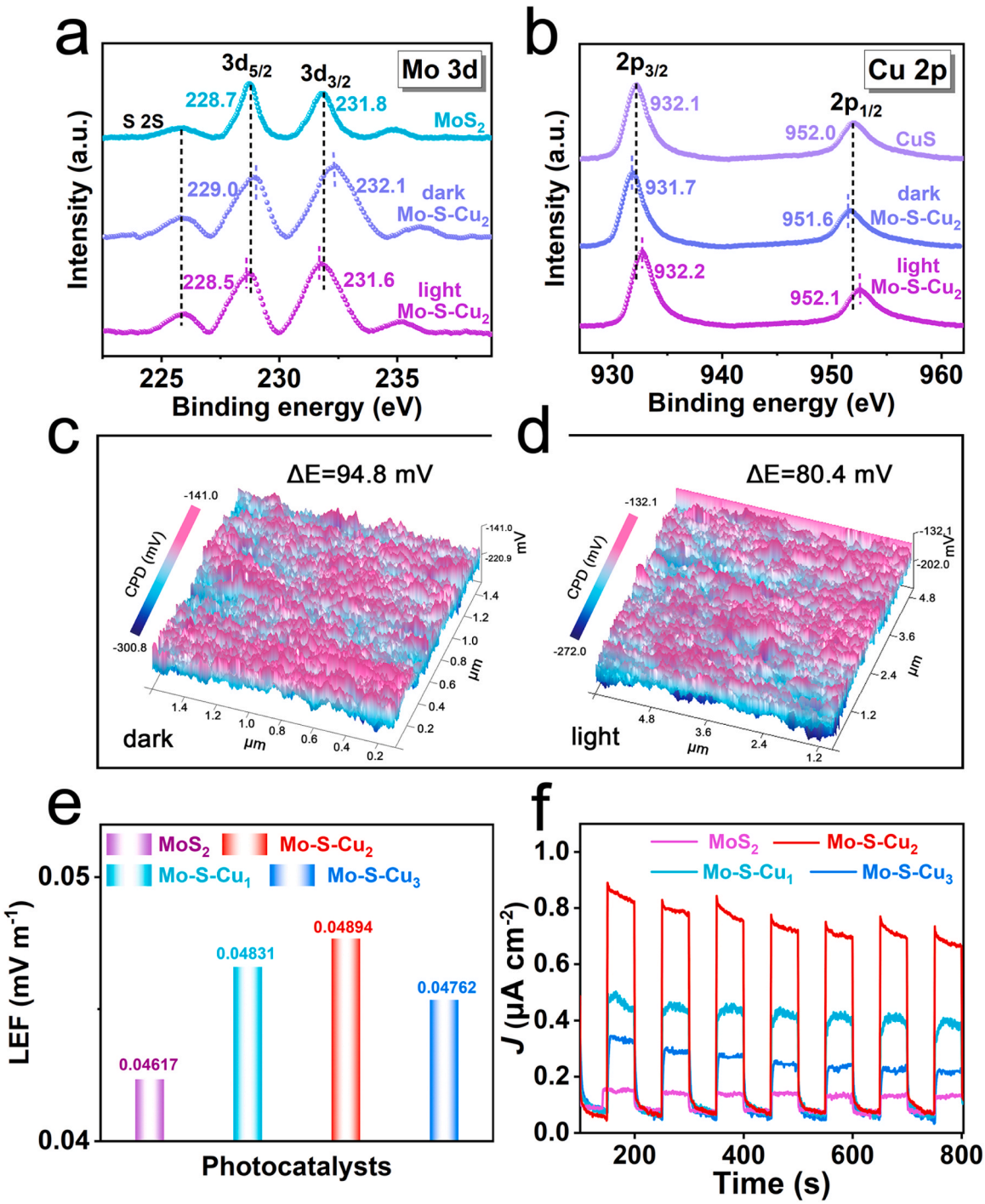

Fig. 2. (a&b) *In-situ* XPS for (a) Mo 3d and (b) Cu 2p detected in dark and irradiation conditions. (c&d) KPFM potential images for Mo-S-Cu_2 in dark (c) and irradiation (d) conditions. (e) The detected polarization field intensities for MoS_2 and Mo-S-Cu samples. (f) Transient photo-current signals.

was dispersed in deionized water by ultrasound, and then certain amounts of $CuSO_4 \cdot 5\ H_2O$ and $Na_2S \cdot 9\ H_2O$ with molar ratio of 1:1 were successively added into MoS_2 dispersion, and CuS was *in situ* grown on MoS_2. After stirring for 20 min, washing and dehydration, the obtained samples were named as Mo-S-Cu_1, Mo-S-Cu_2 and Mo-S-Cu_3 corresponding to the atomic content of Cu in Mo-S-Cu as 10.2 at%, 20.4 at%, and 32.5 at%, respectively (Table S1). Pristine CuS was prepared by the same method process in absence of MoS_2.

2.2. Photocatalytic test for H_2O overall splitting

Photocatalytic H_2O overall splitting was performed in a sealed three-necked flask. Specifically, as follows: N_2 gas was introduced into a three-necked flask including H_2O and a certain amount of photocatalyst to discharge O_2 gas in the photocatalytic system for 60 min, and then the flask was fast sealed with film. After soon, the sealed photocatalytic system equipped with reflux condensation was illuminated under PLSSXE300 with a cut-off filter ($\lambda \geq 400$ nm). In situ and online chromatographic detection system (GC-2014, Shimadzu, TCD) was performed to identify products. STH has been tested under a 300 W Xe lamp

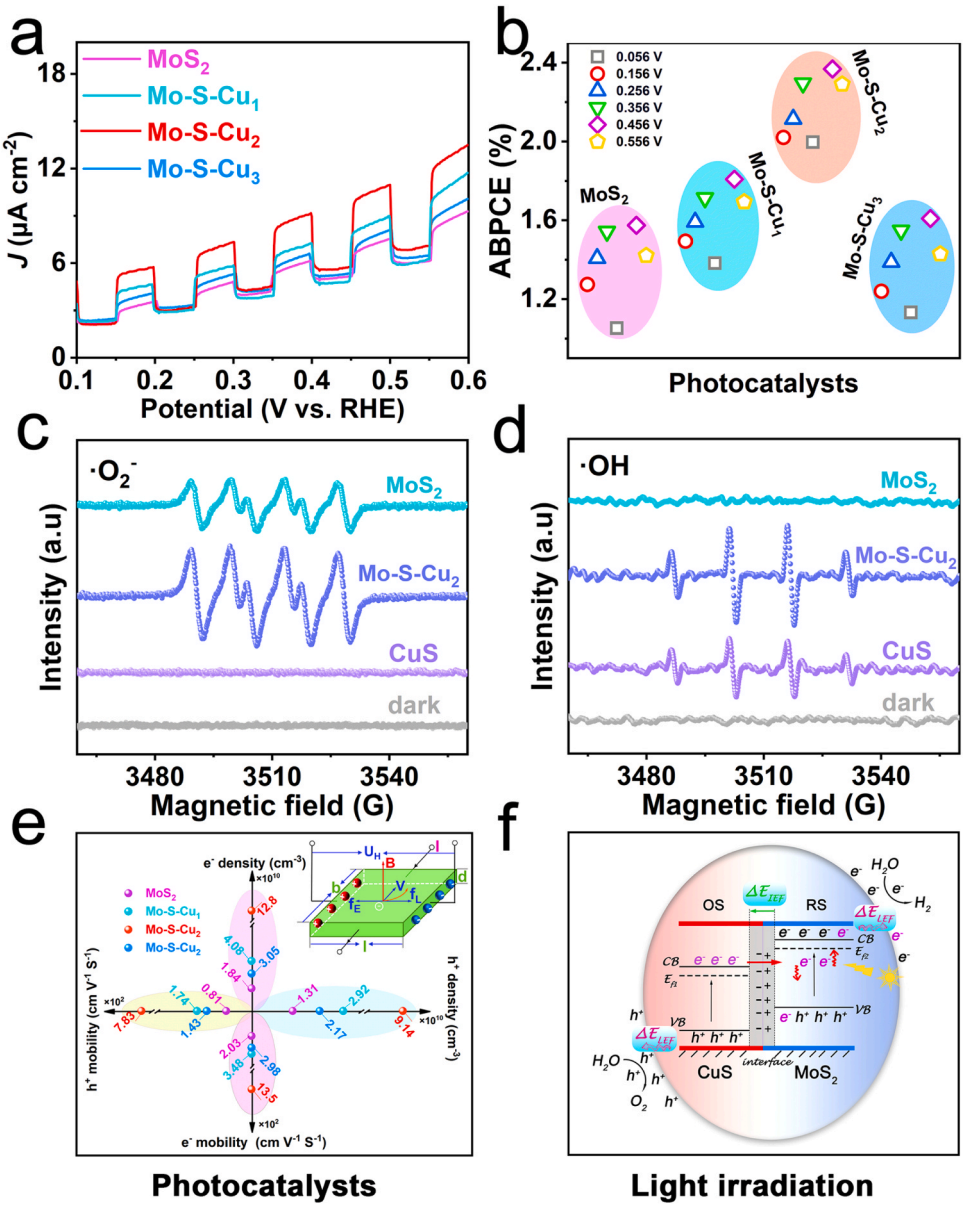

Fig. 3. (a) Transient Chopped $J-V$ curves and (b) the derived ABPCE values. (c&d) *In-situ* EPR spectra for (c) DMPO-•$O_2^-$and (d) DMPO-•OH. (e) Hall effect parameters for mobility and density of e^- and h^+ and the scheme for measurement mechanism. (f) The proposed advanced S-scheme heterojunction mechanism for charge separation and transfer to redox sites.

(PLS-SXE300, Perfect Light) equipped with a reflection filter and AM 1.5 G filter and calculated in light of Equation S1 ($\xi = (A \times \Delta G^0)/(W \times S) \times 100\%$, A, ΔG^0, W, and S are H_2-generation rate (mol/s), 237.13×10^3 J/mol, 0.1 W/cm^2 for irradiation power, and 2.25 cm^2 for irradiated area, respectively). AQE was also tested under the 300 W Xe lamp equipped with bandpass filters in combination with Equation S2 ($\S = (\Delta \times N/\theta) \times 100\%$, Δ, N, and θ represent 4 for coefficient of heterojunction, H_2 molecular amount, and photon amount), and photon amount was trapped by fiber spectrometer (AvaSpec-ULS2048XL-EVO). Specific calculation processes for STH and AQE are shown in Supplementary materials.

3. Results and discussion

3.1. Apparent morphology and microstructures

MoS_2 microfiber samples with diameter of ~0.5 μm and length of ~2 μm are completely comprised of tulle-liked MoS_2 sheets, as recorded by field emission scanning electron microscopy (FESEM) and transmission electron microscope (TEM) (Fig. 1a&d). The morphology of Mo-S-Cu presents no much difference to that of MoS_2 in FESEM image (Fig. 1b), and Mo, S, and Cu are uniformly distributed throughout the sample (Fig. 1c). While TEM image for Mo-S-Cu sample has high contrast due to the existence of many dark areas within the tulle-like morphology, and the higher the CuS content, the greater the contrast (Fig. 1 g, Fig. S1a-c). In high resolution TEM (HRTEM), MoS_2 exposes a wide lattice fringe of 0.631 nm for (002) facet of hexagonal crystal (Fig. 1e&f) [24]. Comparatively, for Mo-S-Cu, the continuous and wide lattice stripes of MoS_2(002) are interspersed by some small lattices with interplanar spacing of 0.281 nm which is hexagonal CuS(103) facet (Fig. 1 h&i, Fig. S1d) [25]. Through a precipitation method at room temperature, CuS presents an ordered atomic arrangement, and with increasing CuS content, the intensity of characteristic peaks for CuS increases gradually in X-ray diffraction patterns for Mo-S-Cu samples (Fig. S1e). The easily growing CuS in order on MoS_2 should be attributed to the bridging effect of S locus in MoS_2 during nucleation and

crystallization processes, which should also be favorable to transfer electron between CuS and MoS_2 within Mo-S-Cu heterojunction. Then, the behavior for electron transfer within the constructed Mo-S-Cu was revealed by *in situ* X-ray photoelectron spectroscopy (XPS) (Fig. 2a&b). It is seen that two primary peaks of Mo 3d in pristine MoS_2 at 228.7/231.8 eV belong separately to Mo $3d_{5/2}$ and Mo $3d_{3/2}$ [26], while after CuS grows, these two peaks shift positively to 229.0/232.1 eV in Mo-S-Cu_2, respectively. On the contrary, the two peaks of Cu $2p_{3/2}$ and Cu $2p_{1/2}$ move negatively from 932.1/952.0 eV in the pristine CuS to 931.7/951.6 eV in Mo-S-Cu_2, respectively [27]. The positive or negative shift in binding energy of Mo or Cu demonstrates the electron donor or acceptor characteristics of MoS_2 or CuS in Mo-S-Cu_2 heterojunction due to their Fermi level difference. In accordance with Equation of $h\nu = E_k + E_b + \Phi$ ($h\nu$: incident photon energy; E_k: photoelectron kinetic energy, E_b: electron binding energy, and Φ: work function), Φ for MoS_2 or CuS corresponds to 6.17 eV or 7.90 eV from valence band (VB) spectrum in XPS, and thus MoS_2 shows a lower Φ but a higher Fermi level than CuS (Fig. S2a) [28,29]. Under irradiation (Fig. 2b), the binding energies of Mo $3d_{5/2}$ and Mo $3d_{3/2}$ in Mo-S-Cu_2 shift negatively by ~0.5 eV to 228.5/231.6 eV, while those of Cu $2p_{3/2}$ and Cu $2p_{1/2}$ shift positively by ~0.5 eV to 932.2/952.1 eV compared with the original results obtained in dark. Moreover, the binding energies of S as bridging sites show almost same for Mo-S-Cu_2 in dark or under irradiation (Fig. S2b). It is noted that, semiconductors have been exchanging heat energy from the outside to establish temperature gradients, and they are not adiabatic. After MoS_2 links CuS through S as the electron transport bridge, electrons transfer from MoS_2 with high Fermi level to CuS with low Fermi level *via*. the S bridge under the action of their Fermi difference. In this case, electron transfer behavior results in two effects: on the one hand, the exchanged heat energy leads to the diffusion of charge carriers from the high-temperature region (*i.e.*, interface) to the low-temperature region (surface), which induces the generation of LEF by aggregating positive and negative charges separately. On the other hand, Fermi energy level for OS is close to the center of its band gap, and the one for RS is close to its conduction band (CB) in light of Einstein relationship for heterojunction, thus the Fermi energy levels for the heterojunction in non-adiabatic system are not even in equilibrium, maintaining IEF in interface and LEF on surface. The positive and negative charge localization is presented by the ubiquitous surface potential change in KPFM characterization [30–32]. As the atomic force probe streaks across the surface of Mo-S-Cu, the potential on the surface of the sample has been fluctuating and the highest surface potential difference is tested to be 94.8 mV (Fig. 2c and Fig. S3a-c). Under irradiation, by changing the carrier concentration distribution, the photovoltaic effect is generated to offset IEF influence [33,34], *i.e.*, e^- from VB of CuS are excited to CB and then migrate back to MoS_2 through S as bridges (Fig. S2c-f). Consequently, the detected maximum surface potential difference in KPFM decreases to 80.4 mV (Fig. 2d and Fig. S3d-f). Meanwhile, the formed LEF within the whole system has been tested by polarization tests (Fig. S4a&b) [35,36]. In Fig. 2e, the electric field intensity increases gradually from 0.04617 of the pristine MoS_2 to 0.04831, 0.04894 and then decreases to 0.04762 with loading CuS nanoparticles of 10.2 at%, 20.4 at%, and 32.5 at% on MoS_2, respectively (Fig. 2e). Excessive CuS loading hence can lead to insufficient coordination sites of MoS_2 crystal plane, which increases interface potential barrier, and damages the separation of positive and negative charges and thus the strength of LEF. Under the action of LEF, the optimized S-scheme Mo-S-Cu heterojunction photocatalysts show a significantly enhanced charge separation efficiency and thus a photon-charge conversion capability reflected as the obvious and strong photo-current density in *in situ* photo-current curves (Fig. 2 f) and chopped J-V curves (Fig. 3a) as well as the weakened intensity of fluorescence emission spectra (Fig. S4c) [37,38]. In the applied bias photon-to-current efficiency (ABPCE) (Fig. 3b) derived from the chopped J-V curves, Mo-S-Cu samples exhibit the much more obvious photo-current density compared with that of the other samples. Meanwhile, in *in situ* electron paramagnetic resonance (EPR) under irradiation (Fig. 3c&d), both superoxide ($\cdot O_2^-$) and hydroxyl radicals ($\cdot OH$) signals over Mo-S-Cu_2 are obtained with stronger intensities than that over pristine MoS_2 or CuS which has only one weak adduct signal. It hence can be confirmed that under irradiation, charge transfer in direction and separation in space have been realized smoothly, and e^- from CB of MoS_2 and h^+ from VB of CuS with strong redox abilities can be preserved and transferred to surface for utilization in redox reactions during solar energy conversion. Furthermore, the Hall effect measurements can reveal the generation capability and transfer efficiency of e^- and h^+ over the S-scheme heterojunction by adding Lorentz forces to e^- and h^+ in the magnetic field, which results in the accumulation of positive and negative charges in the direction of perpendicular to the current and magnetic field [39,40]. In Fig. 3e, the charge density for e^- is much more than that for h^+ over the optimal S-scheme Mo-S-Cu_2 heterojunction, with a faster Hall mobility rate and a lower resistivity in comparison with those over pristine MoS_2 and CuS (Fig. S4d). On the basis of these results, it can be proposed that a part of photo-irradiated e^- from CB of CuS recombine with h^+ in VB of MoS_2, and the residual e^- are excited and transferred to CB of MoS_2 due to the Boltzmann distribution characteristics of e^- and h^+ in semiconductors. Therefore, an innovative S-scheme heterojunction photocatalytic system is proposed (Fig. 3f). It includes three stages, *i.e.*, firstly, under the light excitation with sufficient energy, e^- transit from the VB of CuS to CB, and further move to the MoS_2 phase through S bridges due to the driving force of IEF induced by the Fermi level difference; Next, a partial of these e^- have an initial tendency to combine with h^+ of VB in MoS_2, while some of them further transit to CB of MoS_2 for further reaction, reflected by Hall effect tests; Finally, e^- and h^+ migrate smoothly and separately to MoS_2 reductive sites and CuS oxidative sites for redox reaction under the action of LEF in bulk and on their surface.

CuS(103) and MoS_2(002) as the high index oxidative and reductive crystal facets, have low coordination saturation and narrowed *d*-band, resulting in the increase of interatomic wave function overlap between two facets with S as bridges and raising the *d*-band center, which is conducive to improve the chemical adsorption strength and activation of oxyhydrogen and *H intermediates for O_2 and H_2 generation [41]. Thus corporation of MoS_2(002) and CuS(103) can adjust *d*-band center and reduce the overpotential in H_2O splitting process for H_2 and O_2 efficiently releasing. Subsequently, H_2O splitting under continuous bias voltages is performed dynamically over Mo-S-Cu with an improved hydrophilicity, high electro-chemical active area and specific area (Figs. S5&6a-h, Table S2). It is shown that H_2O splitting reaction can occur at a much low onset potential of − 0.041 V *vs.* RHE over the optimal Mo-S-Cu_2 compared with − 0.187 V over MoS_2 in linear sweep voltammogram (LSV) curves (Fig. S6a). In light of the Tafel value of 144 mV dec^{-1} derived from LSV curves (Fig. S6i), proton adsorption from Volmer step is revealed as the rate-determining process in H_2O splitting reaction [42]. As a result, photo-generated e^- and h^+ can realize spatial separation and directional migration to the surface redox active sites in dynamics along with the lowered surface reaction overpotential over the S-scheme Mo-S-Cu heterojunction, which is suitable for the photocatalytic H_2O overall splitting into H_2 and O_2.

3.2. Efficiency for photocatalytic H_2O overall splitting

Under precisely determining experiment conditions of photocatalytic H_2O splitting reaction, *e.g.*, H_2O purity, reactor transmittance, irradiation area, and cooling system (Fig. S7a, Table S3), photocatalytic performances were tested under the assistance of sacrificial agents (0.35 mol/L of Na_2S and 0.25 mol/L of Na_2SO_3) with photocatalyst weight of 30 mg. It is seen that all samples present H_2 evolution capabilities and Mo-S-Cu_2 is the optimal one (Fig. S7b). Thereafter, weight influence of S-scheme Mo-S-Cu heterojunction on photocatalytic activity for H_2O splitting was investigated by using Mo-S-Cu_2 as an instance. H_2- and O_2-generation rates increase obviously with using a dose from 30 to 60 mg, and then the growing rates for H_2 and O_2 generation become

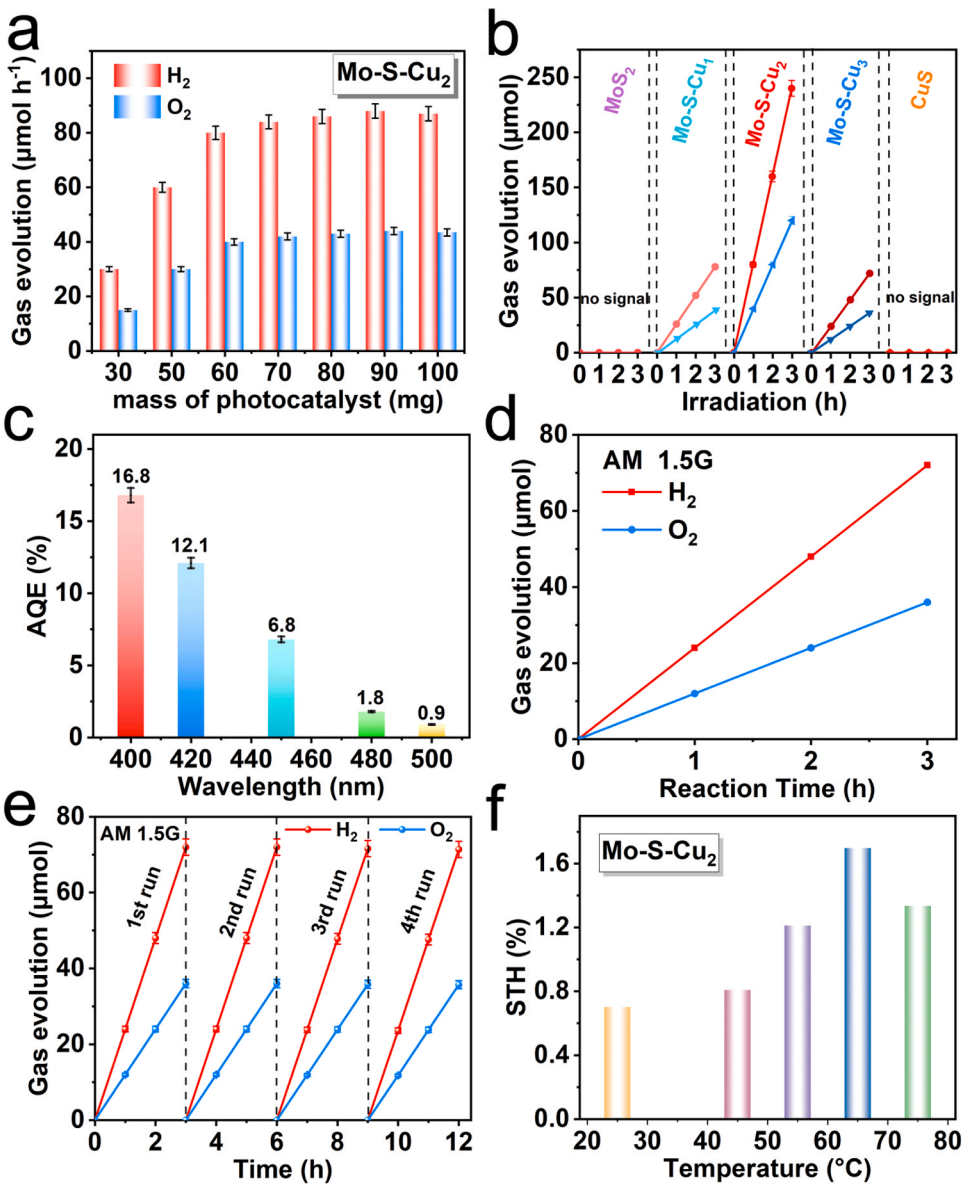

Fig. 4. (a) Mass effect on photocatalytic performance for H_2O overall splitting over Mo-S-Cu_2 system. (b) Photocatalytic H_2O overall splitting under visible light irradiation ($\lambda \geq 400$ nm). (c) AQE values under different wavelengths. (d) Gas yields *vs.* reaction time over Mo-S-Cu_2 under AM 1.5 G irradiation at room temperature. (e) Recycling tests for photocatalytic H_2O splitting over Mo-S-Cu_2 under AM 1.5 G irradiation. (f) STH tests at different temperatures under AM 1.5 G irradiation.

slow and almost stagnant with further enhancing the weight from 70 to 100 mg (Fig. 4a). For the first weight scope, the delivered photocatalyst in photocatalytic system efficiently enhances photon absorption and favors diffusion behavior of photo-generated charge carrier [43,44]; Nevertheless, excessively-delivered photocatalyst leads to light shielding effect for the second weight scope, thus hindering the conversion of photons into charge carriers [45]. As a result, weight of 60 mg as the optimal mass was used in the follow-up experiments. In Fig. 4b, it is shown that, the evolution rates for H_2 and O_2 with stoichiometric ratio increase along with irradiation time over Mo-S-Cu photocatalysts but with different slopes. At the beginning, with increasing CuS content to 20.3 at%, photocatalytic performance of Mo-S-Cu_2 increases due to the enhanced charge separation capability and LEF strength compared with MoS_2. In detail, H_2/O_2 generation over Mo-S-Cu_2 photocatalyst is proportional to irradiation time with a steep slope, and H_2/O_2 generation efficiencies of 80/40 μmol h^{-1} have been achieved under photon irradiation of $\lambda \geq 400$ nm. However, excessive CuS loading of 32.5 at% in Mo-S-Cu_3 leads to a decreased gas evolution efficiency, which should be attributed to the damaged separation of charges, the decreased strength of LEF as well as interface potential barrier wherein MoS_2 has no sufficient coordination sites for CuS growth orderly. For pristine MoS_2 or CuS, no signals of H_2 over MoS_2 and/or O_2 over CuS were obtained with the same conditions, since the dynamic migration of photo-generated carriers and the issue of high surface overpotential have not been effectively solved for monomer MoS_2 and CuS, yet these issues can all be solved over S-scheme heterojunction. In apparent quantum efficiency (AQE) tests (Fig. 4c), AQE at $\lambda = 400$, 420, 450, 480 and 500 nm over Mo-S-Cu_2 photocatalyst achieve 16.8%, 12.1%, 6.8%, 1.8%, and 0.9%, respectively, demonstrating effective solar photon conversion efficiency. Subsequently, solar photon conversion performances over Mo-S-Cu_2 have also been detected with irradiation of AM 1.5 G, and 24.0/12.0 μmol h^{-1} for H_2/O_2 are obtained, corresponding to STH of 0.7% (Fig. 4d). Furthermore, Mo-S-Cu_2 shows the stable efficiency for solar photon conversion in cyclic tests in combination with its stable chemical components, morphology and optical properties (Fig. 4e, Fig. S7c-f). To explore the increase extent of STH, the temperature effect on STH has been investigated over Mo-S-Cu_2, because H_2 recombination with O_2 is an adverse factor (Fig. S7f) [46]. When temperature increases from 25 to 75 °C, H_2/O_2 evolution rate increase gradually from 24.0/12.0 μmol h^{-1} at 25 °C to 58.0/29.0 μmol h^{-1} at 65 °C and then decrease to 45.6/22.8 μmol h^{-1} at 75 °C. Correspondingly, STH increases from 0.7% to 1.7% and then declines to 1.3%. In the initial stage

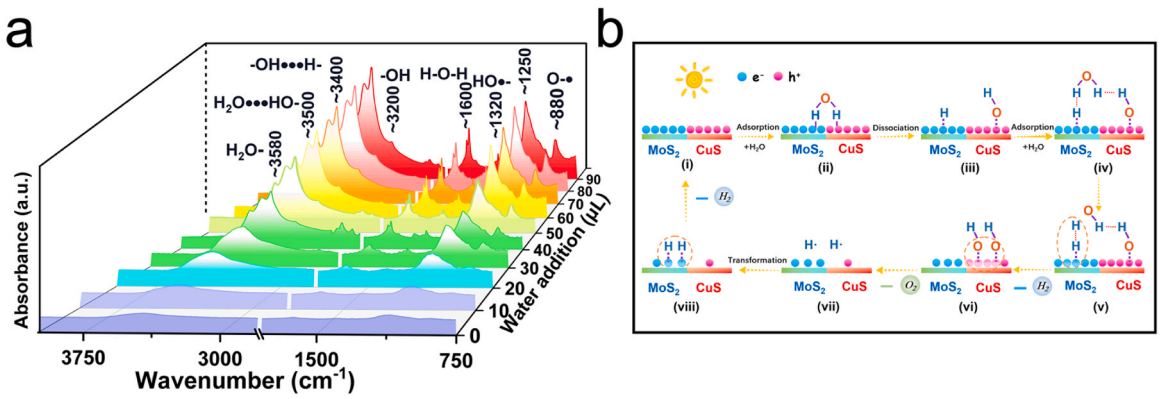

Fig. 5. (a) *In situ* DRIFTS for adding different amount of H_2O over Mo-S-Cu_2, and (b) the proposed photocatalytic mechanism.

of temperature rise, heat energy is conducive to the extrication of the generated H_2 and O_2 from the photocatalyst surface and thus to the re-exposure and utilization of active sites. Nevertheless, much high temperature (*e.g.*, 75 °C) can conversely promote the recombination reaction of H_2 and O_2 to H_2O, which is maybe due to the much-accelerated mass transfer and diffusivity coefficient of H_2 and O_2 in water [47]. Thus, the aim of completing H_2O overall splitting with considerable STH has been successfully achieved over such S-scheme Mo-S-Cu with the optimized charge separation and migration capabilities as well as the lowed surface reaction barrier.

To deeply and accurately understand the dynamic process for photocatalytic H_2O overall splitting into H_2 and O_2, *in situ* DRIFTS was utilized to solve the issue. In Fig. 5a, it is seen that, the peak at ~3580 cm^{-1} is considered as H_2O molecular adsorbing on Mo-S-Cu sample (H_2O-) [48] and signals around ~3500 and ~3400 cm^{-1} are identified as H_2O adsorbing on HO-* (H_2O···HO-*) and * -OH groups interacting with H-bond (*-OH···H-), respectively [49,50]. Signals of * -OH groups with low frequency at ~3200 cm^{-1} and * -OH groups with flexural vibration at ~1320 cm^{-1} can be seen [50]. Signals of ~980 cm^{-1} are induced by the stretching vibration of * -O [51]. In combination with kinetics of charge transfer behavior, generation mechanism of H_2 and O_2 through H_2O splitting over Mo-S-Cu system is proposed (Fig. 5b), *i.e.*, due to the shared ligand S between CuS(103) and MoS_2(002), the interatomic wave function overlap increases and raise the *d*-band centers, which is conducive to the adsorption and activation of H_2O molecules on Mo and Cu atoms·H_2O molecules dynamically tend to be chemically adsorbed and activated into * -H and * -OH on MoS_2 and CuS of Mo-S-Cu (Step iii). Other H_2O molecules continuously interact with *H of MoS_2 and * -OH of CuS *via.* -H bonds (Step iv), and then H_2 molecules are released under the reduction of e^- on MoS_2 (Step v). The remained HO-* groups are oxidized into O_2 molecules with the action of h^+ on CuS (Step vi), and the free state of * -H can be adsorbed further onto MoS_2 and reduced into H_2 by e^- (Step vii).

4. Conclusion

In summary, CuS *in-situ* grown at S sites from MoS_2 has been constructed for H_2O splitting into H_2 and O_2 by increasing the overlap of the wave functions and the density of electron cloud with S as charge transfer bridge to regulate * -OH dehydrogenation on MoS_2 and * -O coupling on CuS, respectively. Photocatalytic H_2O splitting into H_2 and O_2 has been sustainably performed under AM 1.5 G excitation along with STH of 1.70% over the heterojunction photocatalyst. The transfer behavior and the corresponding surface redox dynamical reaction have been revealed with using KPFM, *in-situ* DRIFTS and Hall effect, specifically as follows: i) Fermi levels at interface of MoS_2 and CuS are not equal in non-adiabatic system; ii) IEF synergizing with LEF boost directional transfer of e^- and h^+ to MoS_2 and CuS for dehydrogenating * -OH and subsequently coupling * -O to generate H_2 and O_2, respectively; iii) e^- from CuS partially recombine with h^+ of MoS_2 and further transit to MoS_2 surface for photocatalytic H_2O reduction. This research can provide an in-depth understanding of the charge transfer behavior and kinetic reaction process over heterojunction photocatalysts in non-adiabatic systems, which deepens the universal validity of the S-scheme heterojunction photocatalytic model, facilitating the design and understanding the principles of photocatalysis reasonably.

CRediT authorship contribution statement

Menghan Gan: Conducting experiments, collecting data, writing original draft. **Shanshan Lai:** Conducting supplementary experiments. **Shujuan Jiang:** Ideas, revising manuscript. **Chuanzhi Sun:** Data analysis. **Shaoqing Song:** Ideas, formulation or evolution of overarching research goals and aims.

Declaration of Competing Interest

The authors declare that they have no known competing financial interests or personal relationships that could have appeared to influence the work reported in this paper.

Data Availability

Data will be made available on request.

Acknowledgments

The work was supported with National Natural Science Foundation of China (51972177), Natural Science Foundation of Ningbo City (2021J067), SJLY2021010 of Ningbo University, Fan 3315 Plan, and Yongjiang Scholar Project.

Appendix A. Supporting information

Supplementary data associated with this article can be found in the online version at doi:10.1016/j.apcatb.2023.123278.

References

[1] Q. Wang, K. Domen, Particulate photocatalysts for light-driven water splitting: mechanisms, challenges, and design strategies, Chem. Rev. 120 (2020) 919–985.
[2] S. Dutta, Review on solar hydrogen: Its prospects and limitations, Energy Fuels 35 (2021) 11613–11639.
[3] Q.X. Zhou, Y. Guo, Y.F. Zhu, Photocatalytic sacrificial H_2 evolution dominated by micropore-confined exciton transfer in hydrogen-bonded organic frameworks, Nat. Catal. 6 (2023) 574–584.
[4] D.D. Gao, P.S. Deng, J.J. Zhang, L.Y. Zhang, X.F. Wang, H.G. Yu, J.G. Yu, Reversing free-electron transfer of MoS_{2+x} cocatalyst for optimizing antibonding-orbital occupancy enables high photocatalytic H_2, Evol., Angew. Chem. Int. Ed. 135 (2023), e202304559.

[5] C.B. Bie, L.X. Wang, J.G. Yu, Challenges for photocatalytic overall water splitting, Chem 8 (2022) 1567–1574.
[6] R.A. He, J.R. Ran, Dilemma faced by photocatalytic overall water splitting, J. Mater. Sci. Technol. 157 (2023) 107–109.
[7] P. Zhang, T. Wang, X.X. Chang, J.L. Gong, Effective charge carrier utilization in photocatalytic conversions, Acc. Chem. Res. 49 (2016) 911–921.
[8] S.J. Wan, J.S. Xu, S.W. Cao, J.G. Yu, Promoting intramolecular charge transfer of graphitic carbon nitride by donor-acceptor modulation for visible-light photocatalytic H_2 evolution, Interdiscip, Mater 1 (2022) 294–308.
[9] J.A. Nasir, A. Munir, N. Ahmad, T.U. Haq, Z. Khan, Z. Rehman, Photocatalytic Z-scheme overall water splitting: recent advances in theory and experiments, Adv. Mater. 33 (2021) 2105195.
[10] Q.L. Xu, L.Y. Zhang, B. Cheng, J.J. Fan, J.G. Yu, S-scheme heterojunction photocatalyst, Chem 6 (2020) 1543–1559.
[11] W.K. Chong, B.J. Ng, L.L. Tan, S.P. Chai, Recent advances in nanoscale engineering of ternary metal sulfide-based heterostructures for photocatalytic water splitting applications, Energy Fuels 36 (2022) 4250–4267.
[12] Y.J. Bao, S.Q. Song, G.J. Yao, S.J. Jiang, S-scheme photocatalytic systems, Sol. RRL 5 (2021) 2100118.
[13] L.Y. Zhang, J.J. Zhang, H.G. Yu, J.G. Yu, Emerging S-scheme photocatalyst, Adv. Mater. 34 (2022) 2107668.
[14] J. Anversa, P. Piquini, A. Fazzio, T.M. Schmidt, First-principles study of HgTe/CdTe heterostructures under perturbations preserving time-reversal symmetry, Phys. Rev. B. 90 (2014), 195311.
[15] J.J. Palacios, C. Tejedor, Effects of geometry on edge states in magnetic fields: adiabatic and nonadiabatic behavior, Phys. Rev. B. 45 (1992) 9059.
[16] Y. Kanai, J.C. Grossman, Insights on interfacial charge transfer across P_3HT/fullerene photovoltaic heterojunction from Ab initio calculations, Nano Lett. 7 (2007) 1967–1972.
[17] F. Williams, A.J. Nozik, Solid-state perspectives of the photoelectrochemistry of semiconductor–electrolyte junctions, Nature 312 (1984) 21–27.
[18] X.F. Wang, P. Vasilopoulos, F.M. Peeters, Band structure of a two-dimensional electron gas in the presence of two-dimensional electric and magnetic modulations and a perpendicular magnetic field, Phys. Rev. B 70 (2004), 155312.
[19] T. Banerjee, F. Podjaski, J. Kröger, B.P. Biswal, B.V. Lotsch, Polymer photocatalysts for solar-to-chemical energy conversion, Nat. Rev. Mater. 6 (2021) 168–190.
[20] S.D. March, A.H. Jones, J.C. Campbell, S.R. Bank, Multistep staircase avalanche photodiodes with extremely low noise and deterministic amplification, Nat. Photon. 15 (2021) 468–474.
[21] J. Kosco, S. Gonzalez-Carrero, C.T. Howells, T. Fei, Y.F. Dong, R. Sougrat, G. T. Harrison, Y. Firdaus, R. Sheelamanthula, B. Purushothaman, F. Moruzzi, W. D. Xu, L.Y. Zhao, A. Basu, S.D. Wolf, T.D. Anthopoulos, J.R. Durrant, I. McCulloch, Generation of long-lived charges in organic semiconductor heterojunction nanoparticles for efficient photocatalytic hydrogen evolution, Nat. Energy 7 (2022) 340–351.
[22] X.Y. Zhou, G. Meng, H. Guo, B. Jiang, First-principles insights into adiabatic and nonadiabatic vibrational energy-transfer dynamics during molecular scattering from metal surfaces: The importance of surface reactivity, J. Phys. Chem. Lett. 13 (2022) 3450–3461.
[23] F. Wang, X.P. Wang, Y.F. Zhao, D. Xiao, L.J. Zhou, W. Liu, Z.D. Zhang, W.W. Zhao, M.H.W. Chan, N. Samarth, C.X. Liu, H.J. Zhang, C.Z. Chang, Interface-induced sign reversal of the anomalous Hall effect in magnetic topological insulator heterostructures, Nat. Commun. 12 (2021) 79.
[24] G.J. Yao, S. Yang, S.J. Jiang, C.Z. Sun, S.Q. Song, Spin polarized graphene monolayer of van der Waals heterojunction for photocatalytic H_2O overall splitting, Appl. Catal. B: Environ. 315 (2022), 121569.
[25] C. Wu, W.X. Huang, H.M. Liu, K.L. Lv, Q. Li, Insight into synergistic effect of Ti_3C_2 MXene and MoS_2 on anti-photocorrosion and photocatalytic of CdS for hydrogen production, Appl. Catal. B: Environ. 330 (2023), 122653.
[26] N. Luo, C. Chen, D.M. Yang, W.Y. Hu, F.Q. Dong, S defect-rich ultrathin 2D MoS_2: The role of S point-defects and S stripping-defects in the removal of Cr (VI) via synergistic adsorption and photocatalysis, Appl. Catal. B: Environ. 299 (2021), 120664.
[27] Y.L. Li, Q. Zhao, Y. Zhang, Y.C. Li, L.Z. Fan, F.T. Li, X.H. Li, In-situ construction of sequential heterostructured CoS/CdS/CuS for building "electron-welcome zone" to enhance solar-to-hydrogen conversion, Appl. Catal. B: Environ. 300 (2022), 120763.
[28] X.B. Li, Y. Hu, F. Dong, J.T. Huang, L. Han, F. Deng, Y.D. Luo, C.Z. He, Z.J. Feng, Z. Chen, Y.F. Zhu, Non-noble-metallic Ni_2P nanoparticles modified O_V-BiOBr with boosting photoelectrochemical hydrogen evolution without sacrificial agent, Appl. Catal. B: Environ. 325 (2023), 122341.
[29] X.B. Li, Q. Liu, F. Deng, J.T. Huang, L. Han, C.Z. He, Z. Chen, Y.D. Luo, Y.F. Zhu, Double-defect-induced polarization enhanced O_V-BiOBr/$Cu_{2-x}S$ high-low junction for boosted photoelectrochemical hydrogen evolution, Appl. Catal. B: Environ. 314 (2022), 121502.
[30] R.T. Chen, D.Y. Zhang, Z.Y. Wang, D.F. Li, L.C. Zhang, X.L. Wang, F.T. Fan, C. Li, Linking the photoinduced surface potential difference to interfacial charge transfer in photoelectrocatalytic water oxidation, J. Am. Chem. Soc. 145 (2023) 4667–4674.
[31] S.M. Li, Y.S. Zhou, Y.L. Zi, G. Zhang, Z.L. Wang, Excluding contact electrification in surface potential measurement using kelvin probe force microscopy, ACS Nano 10 (2016) 2528–2535.
[32] C. Yang, S.J. Wan, B.C. Zhu, J.G. Yu, S.W. Cao, Calcination-regulated microstructures of donor-acceptor polymers towards enhanced and stable photocatalytic H_2O_2 production in pure water, Angew. Chem. Int. Ed. 61 (2022), e202208438.
[33] Q.X. Wang, A.T.S. Wee, Upconversion photovoltaic effect of WS_2/2D perovskite heterostructures by two-photon absorption, ACS Nano 15 (2021) 10437–10443.
[34] M.M. Furchi, A. Pospischil, F. Libisch, J. Burgdörfer, T. Mueller, Photovoltaic, effect in an electrically tunable van de Waals heterojunction, Nano Lett. 14 (2014) 4785–4791.
[35] J.R. He, L.J. Hu, C.T. Shao, S.J. Jiang, C.Z. Sun, S.Q. Song, Photocatalytic H2O overall splitting into H2 bubbles by single atomic sulfur vacancy CdS with spin polarization electric field, ACS Nano 15 (2021) 18006–18013.
[36] F.Z. Chen, J. Wang, S. Yang, S.J. Jiang, C.Z. Sun, S.Q. Song, Activating main-group Mg atomic sites within tri-s-triazine for photocatalytic H_2O overall splitting: Dynamic mechanism and performance, ACS Catal. 13 (2023) 5678–5688.
[37] Q.H. Zhang, Y. Xia, S.W. Cao, "Environmental phosphorylation" boosting photocatalytic CO_2 reduction over polymeric carbon nitride grown on carbon paper at air-liquid-solid joint interfaces, Chin. J. Catal. 42 (2021) 1667–1676.
[38] J. Yang, J.F. Jing, Y.F. Zhu, A full-spectrum porphyrin–fullerene D–A supramolecular photocatalyst with giant built-in electric field for efficient hydrogen production, Adv. Mater. 33 (2021) 2101026.
[39] Y.J. Zhang, J.T. Ye, Y. Matsuhashi, Y. Iwasa, Ambipolar MoS_2 thin flake transistors, Nano Lett. 12 (2012) 1136–1140.
[40] Y. Saito, Y. Iwasa, Ambipolar insulator-to-metal transition in black phosphorus by ionic-liquid gating, ACS Nano 9 (2015) 3192–3198.
[41] M.C. Zhang, K.X. Zhang, X. Ai, X. Liang, Q. Zhang, H. Chen, X.X. Zou, Theory-guided electrocatalyst engineering: From mechanism analysis to structural design, Chin. J. Catal. 43 (2022) 2987–3018.
[42] V.M. Nikolic, S.L. Maslovara, G.S. Tasic, T.P. Brdaric, P.Z. Lausevic, B.B. Radak, M. P.M. Kaninski, Kinetics of hydrogen evolution reaction in alkaline electrolysis on a Nicathode in the presence of Ni–Co–Mo based ionic activators, Appl. Catal. B: Environ. 179 (2015) 88–94.
[43] M. Melchionna, P. Fornasiero, Updates on the roadmap for photocatalysis, ACS Catal. 10 (2020) 5493–5501.
[44] S. Cao, L.Y. Piao, Considerations for a more accurate evaluation method for photocatalytic water splitting, Angew. Chem. Int. Ed. 59 (2020) 18312–18320.
[45] Z.L. Wang, T. Hisatomi, R.G. Li, K. Sayama, G. Liu, K. Domen, C. Li, L.Z. Wang, Efficiency accreditation and testing protocols for particulate photocatalysts toward solar fuel production, Joule 5 (2021) 344–359.
[46] P. Zhou, I.A. Navid, Y.J. Ma, Y.X. Xiao, P. Wang, Z.W. Ye, B.W. Zhou, K. Sun, Z. T. Mi, Solar-to-hydrogen efficiency of more than 9% in photocatalytic water splitting, Nature 613 (2023) 66–70.
[47] B. Zhang, Q. Daniel, M. Cheng, L. Fan, L. Sun, Temperature dependence of electrocatalytic water oxidation: a triple device model with a photothermal collector and photovoltaic cell coupled to an electrolyzer, Faraday Discuss. 198 (2017) 169–179.
[48] C.S. Choe, J. Lademann, M.E. Darvin, Depth profiles of hydrogen bound water molecule types and their relation to lipid and protein interaction in the human stratum corneum, *vivo*, Anal. 141 (2016) 6329–6337.
[49] W.J. Guo, J.B. Che, S.Q. Sun, Q. Zhou, Investigation of water diffusion in hydrogel pore-filled membrane via 2D correlation time-dependent ATR-FTIR, Spectrosc., J. Mol. Struct. 1171 (2018) 600–604.
[50] I. Bergonzi, L. Mercury, J.B. Brubach, P. Roy, Gibbs free energy of liquid water derived from infrared measurements, Phys. Chem. Chem. Phys. 16 (2014) 24830–24840.
[51] T. Che, Q. Ding, X.L. Wang, Z.C. Feng, C. Li, Mechanistic studies on photocatalytic overall water splitting over ga2o3-based photocatalysts by *Operando* MS-FTIR spectroscopy, J. Phys. Chem. Lett. 12 (2021) 6029–6033.